

PAPER

Cd-doping effects in Ni–Mn–Sn: experiment and *ab-initio* study

To cite this article: Z Ghazinezhad *et al* 2022 *J. Phys. D: Appl. Phys.* **55** 255001

View the [article online](#) for updates and enhancements.

You may also like

- [Facile Liquid-Phase Synthesis of a High-Performance Cd-Doped ZnO-Quantum-Dot-Based Photocatalyst](#)
Xinli Wang and Jin Li
- [Microstructural, optical and electrical transport properties of Cd-doped SnO₂ nanoparticles](#)
Naseem Ahmad, Shakeel Khan and Mohd Mohsin Nizam Ansari
- [Tuning the electronic hybridization in the heavy fermion cage compound YbFe₂Zn₂₀ with Cd doping](#)
M Cabrera-Baez, R A Ribeiro and M A Avila



The Electrochemical Society
Advancing solid state & electrochemical science & technology

243rd ECS Meeting with SOFC-XVIII

More than 50 symposia are available!

Present your research and accelerate science

Boston, MA • May 28 – June 2, 2023

[Learn more and submit!](#)

Cd-doping effects in Ni–Mn–Sn: experiment and *ab-initio* study

Z Ghazinezhad¹ , P Kameli^{1,*} , A Ghotbi Varzaneh^{1,*} , I Abdolhosseini Sarsari¹ , M Norouzi-Inallu¹ , T Amiri² , D Salazar³ , B Rodríguez-Crespo³ , D Vashaei^{4,5} , T H Etsell² and V Chernenko^{3,6} 

¹ Department of Physics, Isfahan University of Technology, Isfahan 84156-83111, Iran

² Department of Chemical & Materials Engineering, University of Alberta, Edmonton, Alberta T6G 1H9, Canada

³ Basque Center for Materials, Applications and Nanostructures and University of Basque Country, Leioa 48940, Spain

⁴ Department of Electrical and Computer Engineering, North Carolina State University, Raleigh, NC 27606, United States of America

⁵ Department of Materials Science and Engineering, North Carolina State University, Raleigh, NC 27606, United States of America

⁶ Ikerbasque, Basque Foundation for Science, Bilbao 48009, Spain

E-mail: Kameli@iut.ac.ir and ghotbi1130@gmail.com

Received 23 December 2021, revised 7 March 2022

Accepted for publication 18 March 2022

Published 31 March 2022



Abstract

Martensitic transformation (MT), magnetic properties, and magnetocaloric effect (MCE) in Heusler-type $\text{Ni}_{47}\text{Mn}_{40}\text{Sn}_{13-x}\text{Cd}_x$ ($x = 0, 0.75, 1, 1.25$ at. %) metamagnetic shape memory alloys (MetaMSMAs) are investigated, both experimentally and theoretically, as a function of doping with Cd. *Ab-initio* computations reveal that the ferromagnetic (FM) configuration is energetically more favorable in the cubic phase than the antiferromagnetic (AFM) state in undoped and doped alloys as well. Moreover, it is revealed that the alloys in the ground state exhibit a tetragonal structure confirming the existence of MT, in agreement with the experiments. It was indicated, both in theory and practice, that a reduction of the unit cell volume and an increase of the MT temperature as a function of the Cd doping. Indirect estimations of MCE in the vicinity of MT were carried out by using thermomagnetization curves measured under different magnetic fields up to 5 T. The results demonstrated that the doped alloys exhibit enhanced values of the inverse MCE comparable with those of Ni–Mn-based MetaMSMAs. Maximum magnetic entropy change in a field change of 2 T increases from $3.0 \text{ J.kg}^{-1}\text{K}^{-1}$ for the undoped alloy to 3.4 and $5.0 \text{ J.kg}^{-1}\text{K}^{-1}$ for the alloys doped with 0.75 and 1 at.% of Cd, respectively. The inverse and conventional MCE were explored by direct measurements of the adiabatic temperature change under the magnetic field change of 1.96 T. The Cd doping increased the maximum of inverse MCE by nearly 78% from 0.9 K to 1.6 K for the undoped and doped alloys, respectively. The results depicted that Cd doping can effectively tailor the structural, magnetic, and MCE properties of the Ni–Mn–Sn MetaMSMAs.

Keywords: $\text{Ni}_{47}\text{Mn}_{40}\text{Sn}_{13-x}\text{Cd}_x$ ($x = 0, 0.75, 1, 1.25$ at. %) metamagnetic shape memory alloys, magnetocaloric effect, martensitic transformation, metamagnetic materials, *ab-initio* calculations

(Some figures may appear in colour only in the online journal)

* Authors to whom any correspondence should be addressed.

1. Introduction

The necessity of employing environmental-friendly and efficient technologies, such as magnetic cooling, becomes more critical as the adverse effect of global climate change and the importance of energy-saving become more apparent. New materials with magnetocaloric effect (MCE) can potentially replace standard gas-compression refrigeration with magnetic cooling [1]. MCE is the intrinsic thermal response of all magnetic materials to the change of the external magnetic field that is enormously intensified when associated with the second-order magnetic transition or first-order magneto-structural transformation [2, 3]. The discovery of the giant MCE in the $\text{Gd}_5(\text{Si}_2\text{Ge}_2)$ alloy that originated from the first-order magnetostructural phase transition stimulated much effort to develop new magnetic refrigeration materials [2]. Some of the famous first-order compounds with giant MCE are Gd–Si–Ge, Mn–Fe–P–X ($X = \text{As, Ge, Si}$), $\text{La}(\text{Fe, Si})_{13}$, $\text{La}_{1-x}\text{Pr}_x\text{Fe}_{12}\text{B}_6$ ($x = 0.05\text{--}0.2$), Mn–Co–Ge, Fe–Rh and Ni–Mn–Z ($Z = \text{Sn, In, Sb, Ga}$) [4–10].

It is worth to mention that rare earth (RE)-based materials are one of the important branches of MCE materials. $\text{Er}_{20}\text{Ho}_{20}\text{Gd}_{20}\text{Ni}_{20}\text{Co}_{20}$ with wide entropy peak [11], new series of B-site ordered $\text{RE}_2\text{ZnMnO}_6$ ($\text{RE} = \text{Gd, Dy and Ho}$) perovskites [12], B-site half-doped $\text{RE}_2\text{FeAlO}_6$ ($\text{RE} = \text{Gd, Dy, Ho}$) compounds [13], $\text{Gd}_2\text{MgTiO}_6$ [14] and $\text{RE}_6\text{Co}_2\text{Ga}$ ($\text{RE} = \text{Ho, Dy or Gd}$) [15] show suitable potential for cryogenic magnetic refrigeration technology. A combination of RE and transition metals-based alloys sometimes show promising cryogenic magnetocaloric performance like NdGa [16]. More investigation of RE compounds is beyond the scope of this article, but a comprehensive report of different ternary rare-earth $\text{RE}_2\text{T}_2\text{X}$ ($\text{RE} = \text{Gd-Tm}$; $\text{T} = \text{Cu, Ni, Co}$; and $\text{X} = \text{Cd, In, Ga, Sn, Al}$) intermetallic compounds with a wide range of magnetic ordering temperatures can be found in Zhang review article [17].

Ni–Mn-based Heusler alloys, especially the non-stoichiometric Mn-rich compositions of $\text{Ni}_2\text{Mn}_{1+x}\text{Z}_{1-x}$, are attractive MCE materials due to their low-cost, rare-earth-free nature, noticeable values of the magnetic entropy change, ΔS_M , and adiabatic temperature change, ΔT_{ad} [18]. It should be noted that large values of these parameters observed experimentally usually turn out to be a ‘one-time’ effect due to the thermal hysteresis. However, many studies have focused on developing strategies for at least partially overcoming or bypassing the challenge of hysteresis.

These metamagnetic shape memory alloys (MetaMSMAs) are characterized by the mixed ferro- and antiferromagnetic (AFM) interactions between Mn atoms placed at different positions in the unit cells of the crystal lattice [9].

Ni–Mn–Z ($Z = \text{Sn, Sb, In, and Ga}$) compositions, depending on the Mn/Z ratio, display a magnetostructural martensitic transformation (MT) from the high-symmetric austenite phase to low-symmetric martensitic phase resulting in a totally different magnetic state of these phases, due to a strong magneto-structural coupling as one of the reasons [19]. Owing to MT, these materials show multifunctional properties, such

as an inverse MCE, exchange bias effect (EB), magnetoresistance, shape memory effect, etc [20–23]. The structural and magnetic properties of these alloys can be directly tuned by changing the composition or partial doping with the fourth element.

Magnetic properties in these alloys are mainly associated with the magnetic moments of Mn coupled through conduction electrons leading to the long-range indirect Ruderman–Kittel–Kasuya–Yosida (RKKY) exchange interaction [24]. Changing the composition can alter the Mn–Mn distances, which, due to the distance-dependent RKKY interactions, results in a variation of the magnetic state. During the onset of MT, a drastic change of the saturated magnetization occurs, giving rise to the multifunctional properties, such as MCE, exchange bias, etc [25].

In the non-stoichiometric cases, $\text{X}_2\text{Y}_{1+x}\text{Z}_{1-x}$, the regular Mn atoms locate in the Mn sublattices (Mn1), but the extra Mn atoms (Mn2) occupy the Sn sites. This substitution decreases the distance between the closest neighbor Mn atoms, leading to AFM configurations. The magnetic moments between Mn1–Mn1 and Mn1–Mn2 pairs consequently are coupled ferromagnetically (FM) and antiferromagnetically, respectively. Such FM and AFM configurations are in a competition, typical of the non-stoichiometric Ni–Mn-based Heusler alloys [26]. The magnetic state of these alloys additionally depends on the X (Ni, Co, Cu) [27] as well as Z (In, Sn, Ga) elements and can be altered by modifying the magnetic coupling between Mn1 and Mn2 atoms [28–30]. For instance, Sokolovskiy *et al* [31] showed that Co doping instead of Ni could strongly modify the stable magnetic configuration of the cubic austenite phase.

The jump-like change of the magnetization, down to zero, during the forward MT in MetaMSMAs is due to the different magnetic states (for instance, from FM to AFM) because the forward MT is accompanied by the strong enhancement of the AFM interactions resulting from the noticeable reduction in the Mn–Mn distances in the martensitic state [28, 32, 33]. With regards to the competing condition of coupling between Mn1 and Mn2 (FM or AFM), there is still controversy regarding the stable ground state of the Heusler-type Ni–Mn-based MetaMSMAs, as different calculations indicate that both the FM and AFM configurations could be stable. However, whereas the calculation data show that Ni–Mn–In and Ni–Co–Mn–Sn MetaMSMAs should exhibit the FM configuration as more stable than AFM [34, 35], the AFM configuration appeared to be more energetically favorable than FM, e.g. in Zn- or C-doped Ni–Mn–Sn MetaMSMAs [36, 37]. This discrepancy may be attributed to the imperfections of the *ab-initio* methods used; therefore, more elaborated first-principle calculations are still needed to accurately study the complex magnetic configurations and their stability in these alloys. This paper seeks to resolve the aforementioned discrepancies by adding a Hubbard U correction to the computations.

A significant rectification of magnetic properties and MT’s characteristics in Ni–Mn–Z MetaMSMAs is possible by tailoring the composition or adding a fourth element via partial

substitution of Z, Mn, or Ni. This procedure is being abundantly explored in the literature with different MetaMSMAs. Incorporation of d transition metals or other elements in such alloys have a strong impact on the electronic structure and the magnetic exchange interactions, leading to a rich interplay among magnetism, crystal structure, and electronic structure in the course of MT [38]. For instance, adding Co, Cr, or Zn as the $3d$ transition metals or adding Nb as a $4d$ transition metal to Ni–Mn-based MetaMSMAs was perceived as an efficient tool to enhance the magnetic properties [32, 37, 39]. It is worth mentioning that the most published works on this subject are devoted to the effect of $3d$ transition metals. Notably, the MCE properties of Ni–Mn-based MetaMSMAs are tailored by the doping of the fourth element with a predominance of $3d$ transition metals [40, 41].

In the present work, theoretical and experimental investigations of the influence of partial substitution of Sn by Cd, as a $4d$ transition metal, on MT, magnetic properties, and MCE in $\text{Ni}_{47}\text{Mn}_{40}\text{Sn}_{13-x}\text{Cd}_x$ ($x = 0, 0.75, 1, 1.25$ at. %) MetaMSMAs have been performed. The Cd-doping effect has not been considered yet for these alloys in the literature. Another objective for investigating Cd-doping on the Sn site is to compare the influence of partial substitution of Sn with Zn in the same Ni–Mn–Sn alloy, which was considered in our previous work [37]. Zn and Cd have the same number of valence electrons but different atomic radii. Regarding the closeness of MT temperatures in both Cd-doped and Zn-doped Ni–Mn–Sn, the role of the unit cell volume in changing the MT characteristics is clarified. The Cd-doping effect on the MCE properties has been explored by the indirect and direct measurements of the magnetic field-induced entropy change and adiabatic temperature change, respectively.

2. Experimental and computational details

2.1. Experimental methods

Bulk alloys with compositions of $\text{Ni}_{47}\text{Mn}_{40}\text{Sn}_{13}$ (Cd0Sn), $\text{Ni}_{47}\text{Mn}_{40}\text{Sn}_{12.25}\text{Cd}_{0.75}$ (Cd0.75Sn), $\text{Ni}_{47}\text{Mn}_{40}\text{Sn}_{12}\text{Cd}_1$ (Cd1Sn), and $\text{Ni}_{47}\text{Mn}_{40}\text{Sn}_{11.75}\text{Cd}_{1.25}$ (Cd1.25Sn) were prepared by mechanical alloying described in details elsewhere [42]. The powders were compressed and encapsulated in a quartz tube under Ar atmosphere to avoid oxidation during heat treatments. The samples were quenched in cold water after homogenization at 1223 K for 16 h. Phase identification was performed at room temperature by x-ray diffraction (XRD, ASENWARE AW-DX300 diffractometer) using filtered Cu $K\alpha$ radiation ($\lambda = 1.54184$ Å, 40 kV, 30 mA). Magnetization loop measurements were carried out using a SQUID magnetometer (Quantum Design, MPMS-7) under applied magnetic fields up to 5 T. The thermomagnetization curves, $M(T)$, were recorded under an external magnetic field of 0.01 T in the temperature range of 5–350 K using zero-field-cooling (ZFC) and field-cooling (FC) protocols. Direct measurements of MCE, i.e. adiabatic temperature change, ΔT_{ad} , for a magnetic field change of 1.96 T have been conducted via a custom-made adiabatic calorimeter. Details of the experimental setup can be found elsewhere [43].

2.2. Computational method

The computations were performed for selected compositions of MetaMSMAs using a plane-wave-based density functional theory (DFT) within the QUANTUM ESPRESSO package at zero temperature [44]. To employ the projector augmented wave (PAW) pseudopotentials, the following valence electron configurations were used: $4s^2 3d^8 4p^0$ for Ni, $3p^6 4s^2 3d^5$ for Mn, $5s^2 4d^{10} 5p^2$ for Sn, and $5s^2 4d^{10} 5p^0$ for Cd. All pseudopotentials were generated from PS library 0.3.1 employing the Perdew–Burke–Ernzerhof (PBE) exchange–correlation [45]. The non-stoichiometric compositions were simulated employing the supercell approach. The calculations were carried out for the $\text{Ni}_8\text{Mn}_6\text{Sn}_2$ and $\text{Ni}_{16}\text{Mn}_{12}\text{Sn}_3\text{Cd}_1$ supercells containing 16 and 32 atoms generated by VESTA [46]. The Broyden–Fletcher–Goldfarb–Shanno (BFGS) algorithm with a convergence criterion of 102 Ryd/Bohr was used to optimize the lattice parameter of a 16-atom supercell corresponding to L_{21} ordered structure. Subsequently, repeating that in one direction, 32-atoms supercell was obtained. The first one corresponds to the $\text{Ni}_{47}\text{Mn}_{40}\text{Sn}_{13}$ composition and the second one to $\text{Ni}_{47}\text{Mn}_{40}\text{Sn}_{12}\text{Cd}_1$. Furthermore, it was considered that two magnetic configurations during the lattice relaxation, FM, and AFM. For AFM configuration several states can be considered, antiparallel configuration among Mn1 and Mn2 with Ni parallel to Mn1, opposite direction of Mn1 and Mn2 with Ni antiparallel to Mn1, and parallel configuration of Mn1 and Mn2 with Ni antiparallel to them. It was concluded that the AFM interaction between Mn1 and Mn2 while Ni is parallel with Mn1 is more energetically favorable and thus considered for the calculations in this research due to time-consuming computations. A kinetic energy cutoff of 450 eV was employed for the plane-wave expansion. Test calculations with more K-points and higher kinetic energy cutoff values render the same outcomes. The K grid points for the 16-atom supercell were $8 \times 8 \times 8$, whereas it was $8 \times 8 \times 4$ for the 32-atom supercell.

3. Results and discussion

3.1. Experimental results

3.1.1. Crystal structure. MT involves the change of the symmetry and volume of the crystallographic unit cell [47], whereby the knowledge of changes in the crystal structure is essential for interpreting the MT data [48]. Figure 1 shows x-ray diffraction patterns obtained at room temperature. The results of Rietveld refinement (done by a Fullprof software and presented in figure 1) reveal that the alloys Cd0Sn, Cd0.75Sn, and Cd1Sn are in the L_{21} -ordered cubic austenite phase with a space group of $Fm\bar{3}m$, whereas the Cd1.25 alloy exhibits an orthorhombic martensitic structure with a $Pmma$ space group. The ‘superlattice/main peak’ intensity ratio parameter was calculated to estimate the degree of atomic order in these alloys [37]. It is found that the value of the mentioned ratio increases by the Cd doping; therefore, it can be concluded that the degree of L_{21} order is increasing in the austenite phase. The obtained lattice parameters and the calculated unit cells volumes were

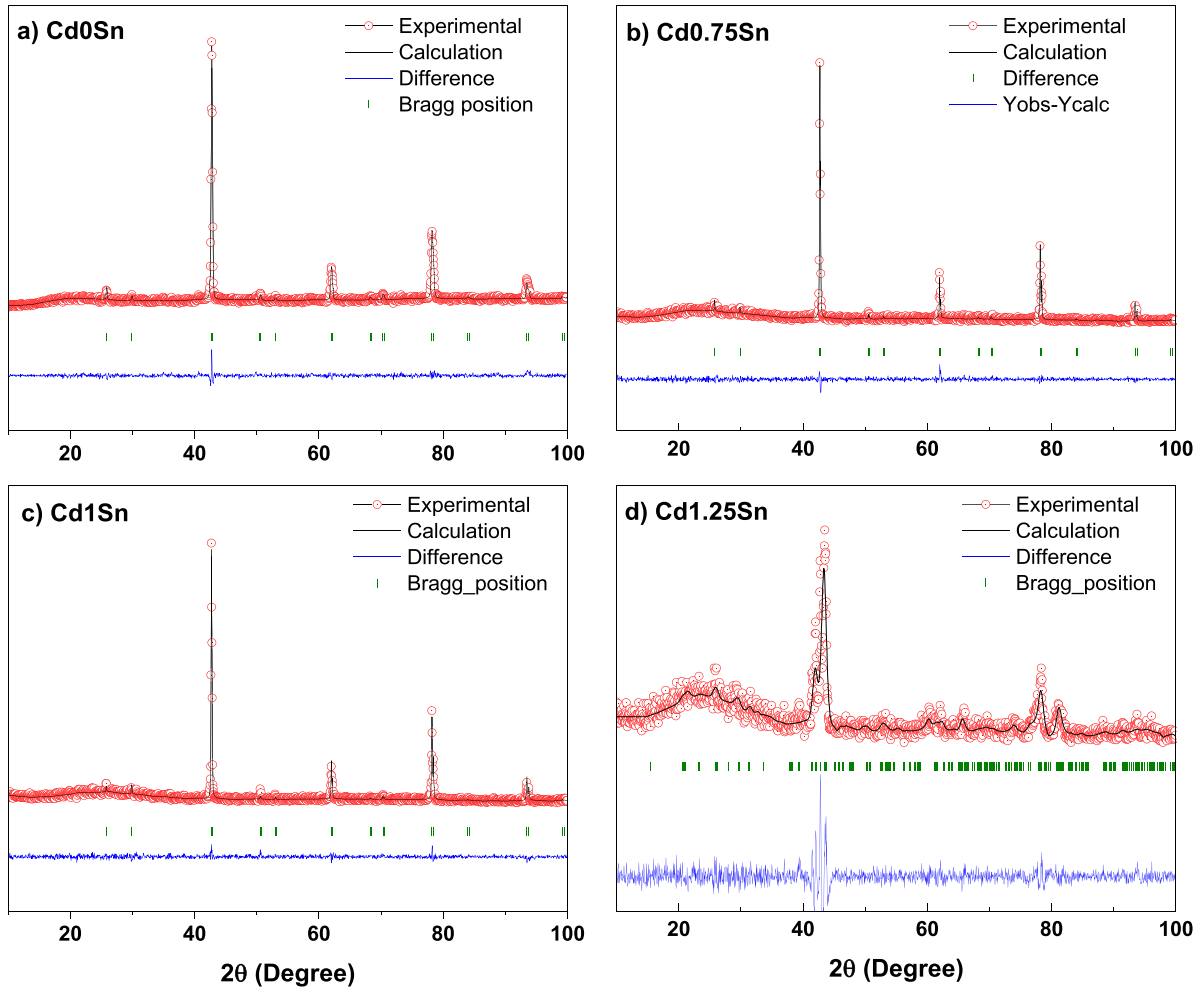


Figure 1. XRD patterns of the Cd0Sn (a), Cd0.75Sn (b), Cd1Sn (c), and Cd1.25Sn (d) alloys at room temperature with the results of FullProf analysis.

Table 1. Crystallographic parameters of the unit cells of the alloys.

Composition	Space group	a (Å)	b (Å)	c (Å)	Unit cell volume (Å ³)
Ni ₄₇ Mn ₄₀ Sn ₁₃	<i>Fm</i> $\bar{3}$ <i>m</i>	5.993	5.993	5.993	215.245
Ni ₄₇ Mn ₄₀ Sn _{12.25} Cd _{0.75}	<i>Fm</i> $\bar{3}$ <i>m</i>	5.985	5.985	5.985	214.384
Ni ₄₇ Mn ₄₀ Sn ₁₂ Cd ₁	<i>Fm</i> $\bar{3}$ <i>m</i>	5.983	5.983	5.983	214.277
Ni ₄₇ Mn ₄₀ Sn _{11.75} Cd _{1.25}	<i>Pmma</i>	8.447	5.713	4.298	206.977
Ni ₄₇ Mn ₄₀ Sn ₁₂ Zn ₁	<i>Fm</i> $\bar{3}$ <i>m</i>	5.979	5.979	5.979	213.740

reported in table 1. The data from table 1 illustrate that the unit cell volume shrinks by increasing Cd content, which is expected since the atomic radius of Cd atom (158 pm) is smaller than that of Sn (225 pm).

3.1.2. Thermomagnetization curves and transformation behavior. Figure 2 shows the temperature dependences of magnetization, $M(T)$, for Ni₄₇Mn₄₀Sn_{13-x}Cd_x ($x = 0, 0.75, 1.00, 1.25$ at.%) alloys under different magnetic fields from 0.1 up to 5 T. Firstly, during cooling from the austenite phase,

the FM transition from paramagnetic to FM state occurs at the Curie temperature of austenite, T_A^C , see figure 4 in the next section. Then, the samples undergo the forward MT accompanied by the large magnetization drop at the magnetostructural transformation temperature, $T_M = \frac{T_M^S + T_M^F}{2}$, where T_M^S and T_M^F are the martensitic start and martensitic finish temperatures, respectively. The reverse MT occurs during heating at $T_A = \frac{T_A^S + T_A^F}{2}$, where T_A^S and T_A^F are the austenitic start and finish temperatures, respectively. The difference $T_A - T_M$ is conventionally accepted as thermal hysteresis of MT; the value $T_0 = (T_M + T_A)/2$ corresponds to the equilibrium MT temperature. MT is a first-order structural transformation from the high-symmetry austenitic phase at high temperature to the low-symmetry martensitic phase at low temperature accompanied by latent heat and specific volume change. During MT, the cubic unit cell undergoes a spontaneous Bain strain by expanding along the principal axis, c , and shrinking in two other directions. As a result, owing to the magnetoelastic interactions, the lower symmetry martensitic phase shows an enhanced magnetocrystalline anisotropy, which reflects in the magnetization curves showing much larger values of anisotropy field [19].

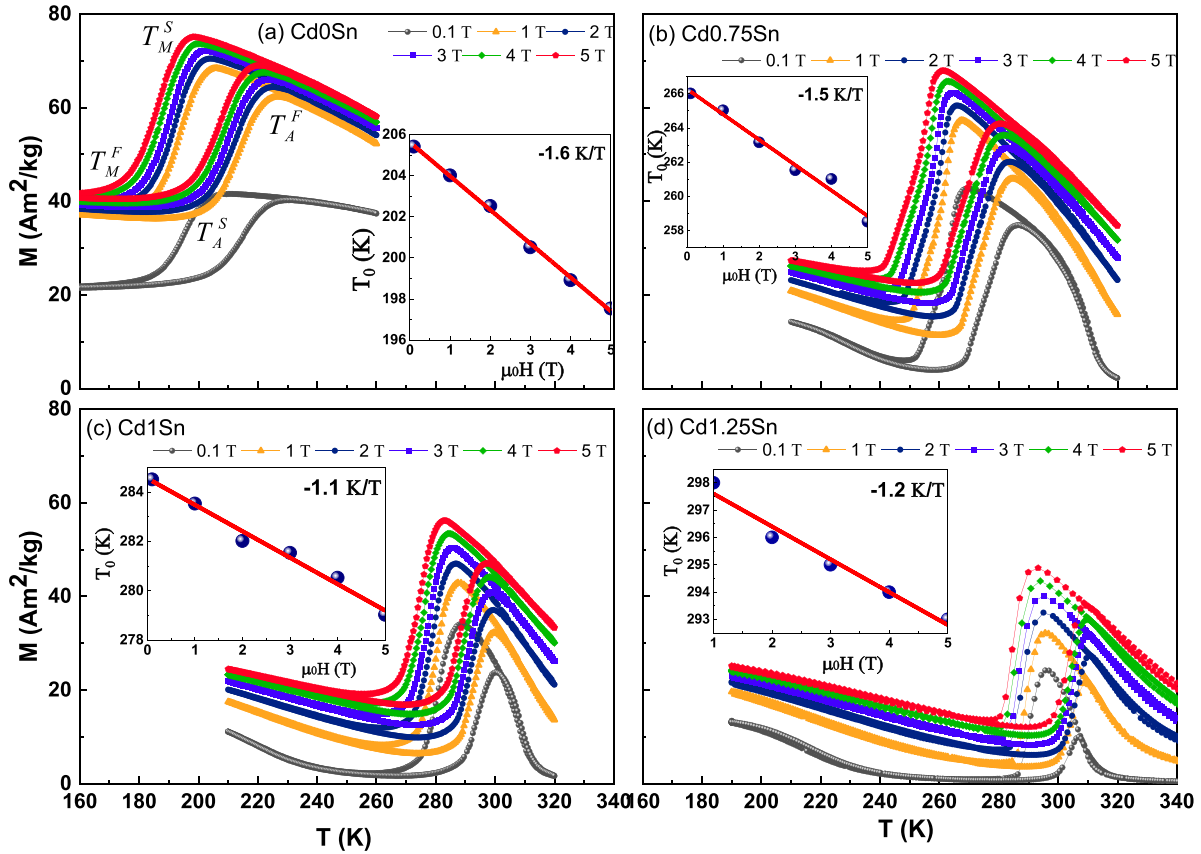


Figure 2. Thermomagnetization curves at different magnetic fields for Cd0Sn (a), Cd0.75Sn (b), Cd1Sn (c) and Cd1.25Sn (d) MetaMSMAs. The characteristic temperatures of martensitic and austenitic start and finish MT are denoted by T_M^S , T_M^F and T_A^S , T_A^F , respectively. The insets show the MT temperature shift as a function of the applied field.

The Curie transition of the martensite occurs at T_M^C (see figure 4 in the next section) as a result of the strengthening of FM correlations in the martensite phase during cooling [49]. Due to a large saturation magnetization drop at the forward MT, the MT temperature appears to be very sensitive to the application of the magnetic field (see figure 2), which is beneficial for the reduction of the field value needed to induce reverse MT and associated giant effects like inverse MCE. The Insets in figure 2 plot the MT temperatures as a function of the magnetic field, showing a linear behavior with a negative slope with a rate, $\frac{dT_0}{d\mu_0H}$. This slope was determined for each sample as shown in the insets of figure 2. High rate of the $\frac{dT_0}{d\mu_0H}$ slope means the possibility to obtain more volume fraction of the austenitic phase transformed from martensite at the lower applied magnetic field [50].

The jump-like change in magnetization, observed in all alloys (figure 2), is lower for the case of the Cd1.25Sn alloy since the FM ordering in the austenite phase is not yet accomplished when MT starts in the cooling process [51].

Zeeman energy depends on the magnetization difference between austenitic and martensitic phases and the magnetic field ($\Delta M \times H$). There is a bigger chance of assisting transformation in the alloys with a higher ΔM as Zeeman energy performs as a driving force to facilitate the field-induced phase transformation [52]. Based on this, it seems that the Cd0.75Sn alloy should transform easier than other alloys in question.

$M(T)$ curves for Cd0Sn show the largest magnetization value in the martensitic phase, indicating that some untransformed part of the austenitic phase still exists at low temperatures, typical behavior of MetaMSMAs [53].

Thermal and/or magnetic hysteresis of MT, as characteristic of the first-order transformation, plays a restrictive role in obtaining the reversibility of MCE in the cooling cycles. The main reason for hysteresis is the energy barrier among austenitic and martensitic phases. Geometric compatibility, which can be obtained from the transformation matrix, is another parameter that controls a hysteresis width. In fact, better compatibility between martensitic and austenitic phases reduces hysteresis. Moreover, this compatibility can be achieved by the change of interatomic distances [54]. The dependences in figure 2 reveal that the thermal hysteresis does not change much by the Cd-doping. Therefore, it can be assumed that the geometric compatibility at the martensite–austenite interfaces in our alloys should be similar [18]. It is worth noting that the influence of the thermal hysteresis on the functional properties of Heusler-type MetaMSMAs can be overcome, to some extent, by utilizing minor loops [55, 56].

The characteristics of MT in MetaMSMAs strongly depend on the composition. Although Cd doping on the Sn sites does not noticeably change the thermal hysteresis, the MT temperature increases significantly, from 200 K for the undoped alloy to near room temperature for doped alloys. This evolution is

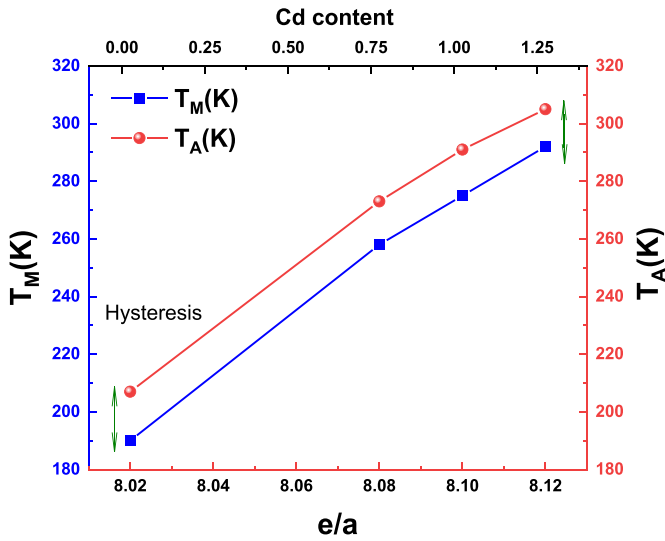


Figure 3. Martensitic ($T_M = T_M^S + T_M^F$) and austenitic ($T_A = T_A^S + T_A^F$) transformation temperatures of Cd-doped alloys as a function of electron concentration. The double arrow shows the hysteresis width of MT.

evident in figure 3. Indeed, this evolution is typical for ternary NiMnZ ($Z = \text{Sn, In, Al, Ga}$) Heusler-type alloys [19]. Several reasons justify this behavior. First, increasing the valence electron concentration (e/a): the higher is the Cd content, the higher is e/a value which, in turn, results in higher values of the transformation temperature. The second efficient parameter affecting MT temperature is a hybridization between Ni 3d and Mn 3d electronic states. A decrease of Sn influences the p - d hybridization between Sn and Mn or Ni, whereby the martensitic state becomes more stabilized [57]. Thirdly, the stabilization of the martensitic state, having a smaller specific volume than austenite, should be produced by reducing the unit cell volume, which is the case of replacement Sn by Cd. The atomic radius of Cd (158 pm) is much smaller than that of Sn (225 pm), which gives rise to a decrease in the cubic lattice parameter of the alloys upon Cd doping (table 1). Reduction in the specific volume brings about shortening the Mn–Mn interatomic distances leading to an enhancement of the AFM interactions in these pairs. This enhancement stabilizes the weakly magnetic martensitic phase, which could be an additional factor contributing to the growth of MT temperature up to room temperature [58]. Furthermore, we try to compare the influence of Cd doping on the Ni–Mn–Sn MetaMSMAs with the results of previously studied Zn doping [37]. The electronic configuration of both Cd and Zn ends by $3d^{10}4s^2$, so both $\text{Ni}_{47}\text{Mn}_{40}\text{Sn}_{12}\text{Zn}_1$ and $\text{Ni}_{47}\text{Mn}_{40}\text{Sn}_{12}\text{Cd}_1$ alloys exhibit the same value of e/a , although the atomic radius of Zn is smaller than that of Cd. In view of the fact that the MT temperature in these two alloys does not have a noticeable difference, thus e/a influences the MT temperature more significantly than the unit cell volume.

3.1.3. Influence of Cd on magnetic properties of alloys. The previous section focused on the influence of Cd doping and

magnetic field on the characteristic temperatures of MT. It was found that MT in the studied alloys is strongly affected by both the magnetic field and the composition. On the other hand, the Curie temperature appeared to be weakly independent of the Cd doping within the composition range explored in the present work. This could mean that the spin-exchange interactions between the regular Mn atoms on their main sites (Mn1) with the neighbors like Mn2 or Ni do not alter significantly by Cd doping instead of Sn.

To get more detailed information about the influence of Cd doping on the magnetic state of the alloys, we measured the low-field magnetization versus temperature using the standard zero-field-cooling (ZFC) and field-cooling (FC) protocols under an applied field of 0.01 T in a wide temperature range. The ZFC state of the samples is probed by heating the samples from 5 K to 320 K. The heating and subsequent cooling dependencies of the magnetization are depicted in figure 4. Owing to 320 K corresponds to a stable temperature of the FM austenite, the $M(T)$ cooling curves do not go to zero at the lowest temperature; a specific finite value remains [59]. The characteristic anomaly near 100 K on the ZFC curves is typically attributed to the blocking temperature, T_B . The second anomaly located near 200 K (the point where the ZFC and FC $M(T)$ curves split) is explained by the coexistence of the FM and AFM interactions [60]. Below blocking temperature, the exchange bias effect (EB) is observed. At higher temperatures (around 220 K), the $M(T)$ downturn in the martensitic state shows an inflection point corresponding to the Curie temperature of the martensitic phase, T_M^C . Above this temperature, the sample reaches a weakly magnetic state. After reverse MT, the final magnetization drop occurs due to the FM to paramagnetic transition around at Curie temperature of austenite, T_A^C [58].

Similar behavior of the low-field thermomagnetization curves has been already observed in different Heusler-type MetaMSMAs, like $\text{Ni}_{50}\text{Mn}_{50-x}\text{Sn}_x$, $\text{Ni}_{50}\text{Mn}_{35}\text{In}_{15}$, $\text{Ni}_{50}\text{Mn}_{25+x}\text{Sb}_{25-x}$, and $\text{Ni}_{43}\text{Mn}_{46}\text{Sn}_{11-x}\text{Ti}_x$, etc [61–64]. For this family of alloys, the ZFC magnetization curve shows a peak around $T \sim 200$ K, below which a large difference exists between ZFC and FC curves. The martensitic phase can disclose different magnetic phases and/or states, such as paramagnetic or AFM phases or mixed FM/AFM and FM/spin-glass states. A variety of possible complex magnetic states comes from the competitive Mn1–Mn1 FM and Mn1–Mn2 AFM interactions which are the origin of the technically important EB effect. The forward MT causes shrinkage of some crystallographic axes, whereby the Mn–Mn separations can decrease [65]. This reduction enhances the strength of AFM interaction in the non-stoichiometric Ni–Mn–Sn Heusler alloys. On the other hand, it was shown that in the stoichiometric Ni_2MnSn , the coupling between Mn1 and Mn2 is FM [66].

3.1.4. Magnetic field induced entropy change. The magnetic entropy change, ΔS_M , versus the external magnetic field is the most frequently used physical quantity to evaluate the MCE indirectly. Another critical parameter that is a more straightforward characteristic of MCE, owing to its direct measurement, is adiabatic temperature change, ΔT_{ad} [53].

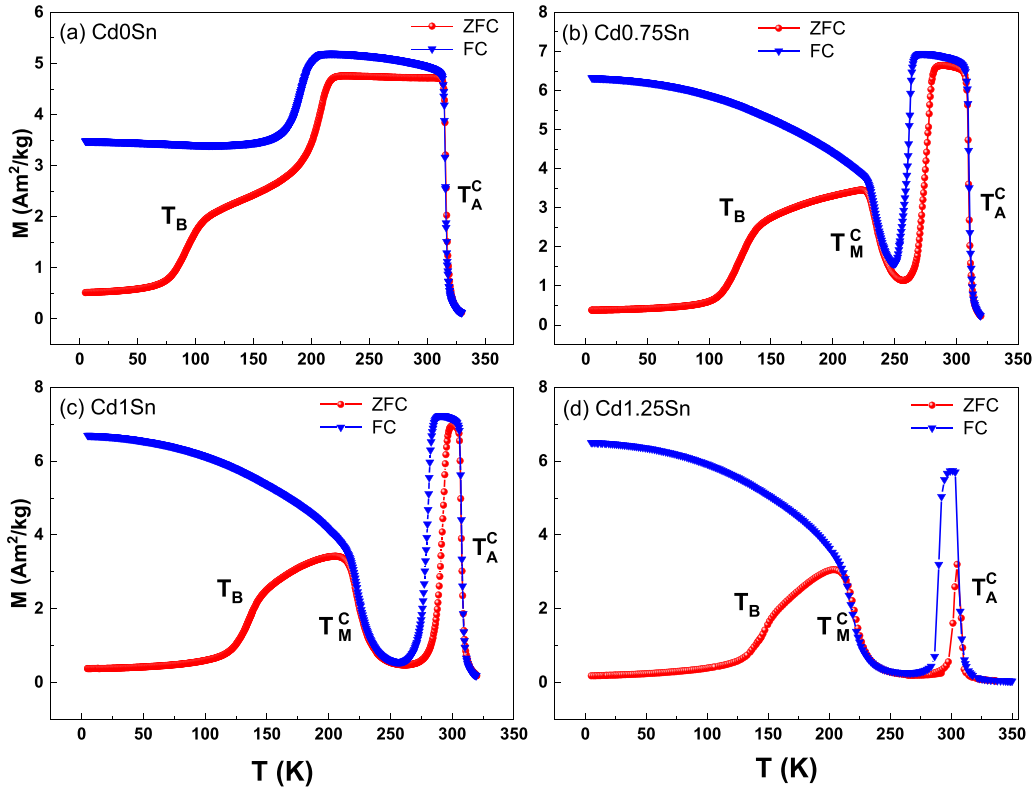


Figure 4. ZFC and FC magnetization curves as a function of temperature for (a) Cd0Sn, (b) Cd0.75Sn, (c) Cd1Sn, and (d) Cd1.25Sn alloys measured at 0.01 T.

ΔS_M as a function of temperature and magnetic field change, ΔH , can be estimated from the thermodynamic Maxwell equation [67]:

$$\Delta S_M(T_j, \Delta H) = \sum_{i=1}^{n-1} \frac{1}{2} \left(\left(\frac{\partial M_i}{\partial T_j} \right)_{H_i} + \left(\frac{\partial M_{i+1}}{\partial T_j} \right)_{H_{i+1}} \right) \Delta H \quad (1)$$

using experimentally measured isofield thermomagnetic curves, $M(T)$, or isothermal magnetization loops, $M(H)$. $M(T)$ dependencies are more reliable to calculate ΔS_M than the family of $M(H)$ curves. Calculations based on $M(H)$ measurements produce artificial spikes on the magnetic entropy change versus temperature curves. These irregularities and overestimations are associated with the specifics of the first-order transformation. Furthermore, $M(H)$ measurements also need a return to the initial martensitic phase after each constant temperature measurement [41, 68].

Figure 5 depicts the temperature dependences of the magnetic entropy change, ΔS_M , under different magnetic fields. The ΔS_M values were determined by equation (1) using $M(T)$ data at the reverse MT presented in figure 2. The curves in figure 5 exhibit the maximums corresponding to the inverse and conventional MCE at MT and the Curie temperature. Under practically meaningful magnetic field change of 2 T, the maximum values of ΔS_M are equal to $3.0 \text{ J}\cdot\text{kg}^{-1}\text{K}^{-1}$ for an undoped alloy and 3.4, 5.0, and $2.8 \text{ J}\cdot\text{kg}^{-1}\text{K}^{-1}$ by increasing the amount of Cd from 0.75, 1–1.25 at.%, respectively. The height of ΔS_M peak around MT depends on the value of the

applied magnetic field, which in practice means that only a partial reverse MT can be induced as a result of its smeared-over-temperature character [69]. Applying higher magnetic fields leads to the increased fraction of martensitic phase converted into austenite, giving rise to a larger inverse MCE for higher fields. The very broad peak above MT is due to the magnetic transition in the austenite phase. Applying higher magnetic fields aligns more magnetic moments along the field direction in the austenite phase, resulting in the increasing absolute values of ΔS_M [70].

The total entropy, ΔS_t , is commonly described as the sum of the following contributions [71]:

$$\Delta S_t = \Delta S_{\text{lat}} + \Delta S_M + \Delta S_{\text{el}}. \quad (2)$$

It has been experimentally illustrated that the electronic contribution (ΔS_{el}) is negligible in Heusler alloys with MT around room temperature [72]. Accordingly, the entropy changes in the lattice (ΔS_{lat}) and the magnetic subsystem (ΔS_M) play the primary role in the total entropy change. The lattice part is stronger than the competing magnetic part, resulting in the inverse MCE. Therefore, the material cools when magnetized adiabatically in the course of reverse MT accompanied by latent heat absorption. On the other hand, its entropy increases when reverse MT is induced under isothermal conditions. The noticeable magnetocaloric performance, together with the rather good mechanical features of Ni–Mn–Sn based MetaMSMAs, originates from a strong p - d covalent bonding [2].

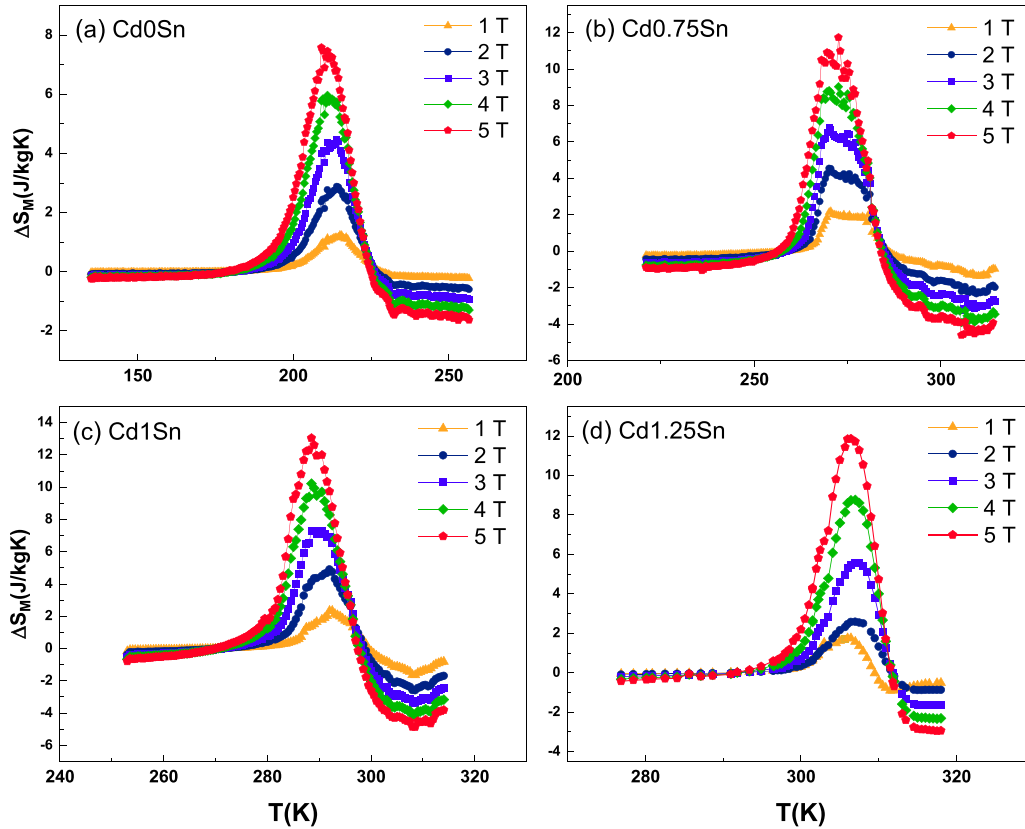


Figure 5. Temperature dependences of the magnetic field induced entropy change under different magnetic fields for Cd0Sn (a), Cd0.75Sn (b), Cd1Sn (c), and Cd1.25Sn (d) alloys.

It is noteworthy that the proportion of the martensite and austenite phases in the samples directly impacts MCE by decreasing the magnetization jump and height of the ΔS_M peaks. This is because the partially induced MT is controlled by the value of the applied magnetic field and the transformation path [73, 74].

For the maximum possible magnetic field induced entropy change, ΔS_{Max} , at the first-order MT, the following equation was deduced in [57]:

$$\Delta S_{Max} = \frac{M_{Sat}}{\partial T_0 / \partial H}, \quad (3)$$

where M_{Sat} and dT_0/dH are saturation magnetization and the magnetic field induced transformation temperature shift, respectively. Equation (3) is reminiscent to the Clausius–Clapeyron relationship. This equation reveals that the optimal values of parameters in the numerator and the denominator should be found to get a maximum entropy change. Although the largest magnetization jump at 2 T is seen in Cd0.75Sn (figure 2), it seems that the competition between these two parameters leads to the Cd1Sn alloy, where an optimal condition for the higher value of magnetic entropy change at 2 T is achieved (figure 5).

3.1.5. Magnetic field induced adiabatic temperature change. ΔT_{ad} at different constant temperatures was measured directly by applying a magnetic field change of 1.96 T

for Cd0Sn and Cd1Sn alloys in the vicinity of reverse MT and Curie temperature of austenite. Direct measurement of ΔT_{ad} is a preferred and trustworthy method to measure MCE. One obstacle of this measurement is that this method requires homemade equipment with suitable adiabatic conditions; thus, experimental data on direct ΔT_{ad} measurements remain hard to find in the literature compared to the indirect ΔT_{ad} measurements [70]. Applying and removing magnetic fields causes the samples to cool and warm, respectively, in the temperature range of MT, showing the inverse MCE. Applying a magnetic field leads to higher values of ΔT_{ad} than removing the field in the vicinity of the forward MT temperature during heating, which is due to the hysteretic losses [75].

Figures 6(a) and (b) illustrates that the doping by Cd essentially increases the maximum of inverse MCE from -0.9 K to -1.6 K for undoped and Cd-doped alloys, respectively. However, at higher temperatures near the Curie temperature, the conventional MCE is observed, as illustrated in figures 6(c) and (d). The Cd doping, in this case, did not enhance the conventional MCE noticeably, which is in line with the already discussed observation of the weak influence of Cd on the Curie temperature of austenite.

For comparison, table 2 depicts the values of the MCE parameters obtained in the present work and other doped and undoped Ni–Mn-based MetaMSMAs taken from the literature.

According to table 2, one may conclude that small Cd-doping is efficient for tuning the MT temperature and

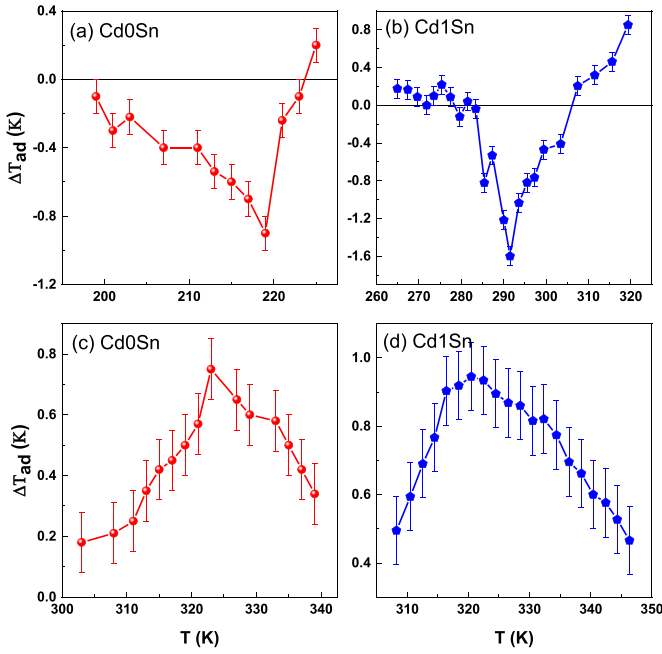


Figure 6. Adiabatic temperature changes as a function of temperature around MT (a) and (b) and magnetic transition (c) and (d) for Cd0Sn (a) and Cd1Sn (b) alloys measured directly under a magnetic field change of 1.96 T during heating.

Table 2. Parameters of the inverse MCE obtained under a field of approximately 2 T for the materials studied in the present work compared with the literature results for other MetaMSMAs compositions.

Alloy composition	$ \Delta T_{ad} $ (K)	$\mu_0 \Delta H$ (T)	T_0 (K)	Reference
Ni ₄₇ Mn ₄₀ Sn ₁₃	0.9	1.96	199	This work
Ni ₄₇ Mn ₄₀ Sn ₁₂ Cd ₁	1.6	1.96	291	This work
Ni ₅₀ Mn ₃₅ In ₁₅	1.6	1.7	302	[43]
Ni _{51.2} Mn _{35.1} Sn _{13.7}	1.1	1.93	300	[47]
Ni _{45.0} Mn _{31.5} Al _{18.5} Co _{5.0}	0.1	1.93	325	[47]
Ni ₄₇ Mn ₄₀ Sn ₁₂ W ₁	1.1	1.96	301	[68]
Ni ₄₇ Mn ₄₀ Sn _{12.5} Cu _{0.5}	0.6	1.8	275	[50]

improving the magnetocaloric properties of the Ni–Mn–Sn MetaMSMAs alloys.

3.2. Computations

A theoretical study was carried out to provide a deeper insight into the role of the Cd dopant for the magnetic and MT characteristics of Ni–Mn–Sn alloys. We performed *ab initio* computations using the Hubbard U correction tool and the supercell approach, as described below.

Figure 7(a) indicates the stimulated 16-atom supercell of the Ni₈Mn₆Sn₂ (formula unit) alloy with the L₂₁ structure. The lattice of fully stoichiometric Heusler alloys, X₂YZ, contains four sublattice sites with the following Wyckoff positions: A (0.25, 0.25, 0.25) and B (0.75, 0.75, 0.75) occupied by X, C (0, 0, 0) by Y, and D (0.5, 0.5, 0.5) by Z [28]. Mn atoms occupy the (0, 0, 0) Wyckoff positions; Sn atoms locate at the (0.5, 0.5, 0.5) Wyckoff position, while Ni atoms prefer to occupy

the (0.75, 0.75, 0.75) and (0.25, 0.25, 0.25) Wyckoff positions, similar to the main group elements in classical Heusler alloys [76]. It is well-known that the site substitution behavior in the intermetallics is determined by the electronic rather than size factor considerations. The site preference of atoms creates a possibility of anti-site disorder in the intermetallics, which can strongly impact their properties. The study of the site preference may be meaningful [77], but this is beyond the scope of the present article.

The arrows in figure 7(a) show the FM state with parallel magnetic moments, one of the two most probable magnetic configurations. FM coupling occurs between atoms pairs located in the Mn1–Mn1 and Ni–Mn1 positions, whereas the AFM interaction occurs between Mn1 and Mn2. As mentioned earlier, the favorable magnetic state can be changed by the variation of X and Z elements. The 32-atoms supercell was considered for the Cd-doped alloy (Ni₁₆Mn₁₂Sn₃Cd₁). To be more precise, a large supercell with 64-atoms should be considered. In the beginning, a supercell with 64 atoms which also fits its content was used, but regarding the magnetic moments and equilibrium lattice parameters, the unit cell with 32 atoms provided almost the same results as the larger cell; therefore, the smaller supercell (32-atom supercell) was used for the doped alloy due to less time-consuming computations.

Ni₂MnSn has the L₂₁-ordered cubic crystal structure. Ni atoms are at the body-centered position of the CsCl-type cubic sublattice, and the corners are filled alternately by Mn and Sn atoms. Consequently, the Mn–Ni–Sn chains are formed along the [111] direction of the cube. In non-stoichiometric cases, the Mn–Ni–Mn chains, due to the occupation of excess Mn atoms in the Sn sublattice (Mn2), are encountered alongside already existing Mn–Ni–Sn chains. The presence of local structural distortions in the non-stoichiometric case causes the enhancement of the Ni 3*d*–Mn 3*d* hybridization. As Priolkar *et al* [78] proposed, the spin superexchange-type interactions develop in the Mn–Ni–Mn diagonal formed due to Mn2 atoms occupying the Sn sublattice.

Furthermore, the intrinsic and the externally forced local structural distortions must strengthen the AFM interactions. The Ni atoms located between Mn and Sn atoms manifest FM interaction with Mn, whereas Ni atoms placed between two Mn atoms align with their spins in the opposite direction. Hence, the Ni moment decreases noticeably since every substituted Sn affects the nearest neighbor Ni sites. Consequently, the magnetic moments of Ni are considerably reduced in the non-stoichiometric case compared to Ni₂MnSn. If the AFM interactions were purely RKKY type between Mn atoms, the Ni moment would not have decreased drastically. The strong evidence of Ni participation in the AFM interactions is the observation of shifted hysteresis loops in the non-stoichiometric case, known as an exchanging bias effect observed in the magnetization measurements [78].

Table 3 depicts the computed and experimental parameters, such as the lattice constants and the total and individual atom magnetic moments in the AFM and FM configurations. Concerning the competition between AFM and FM configurations, theoretical studies mentioned in the literature indicate that the AFM state is stable for the cubic phase; however, it does

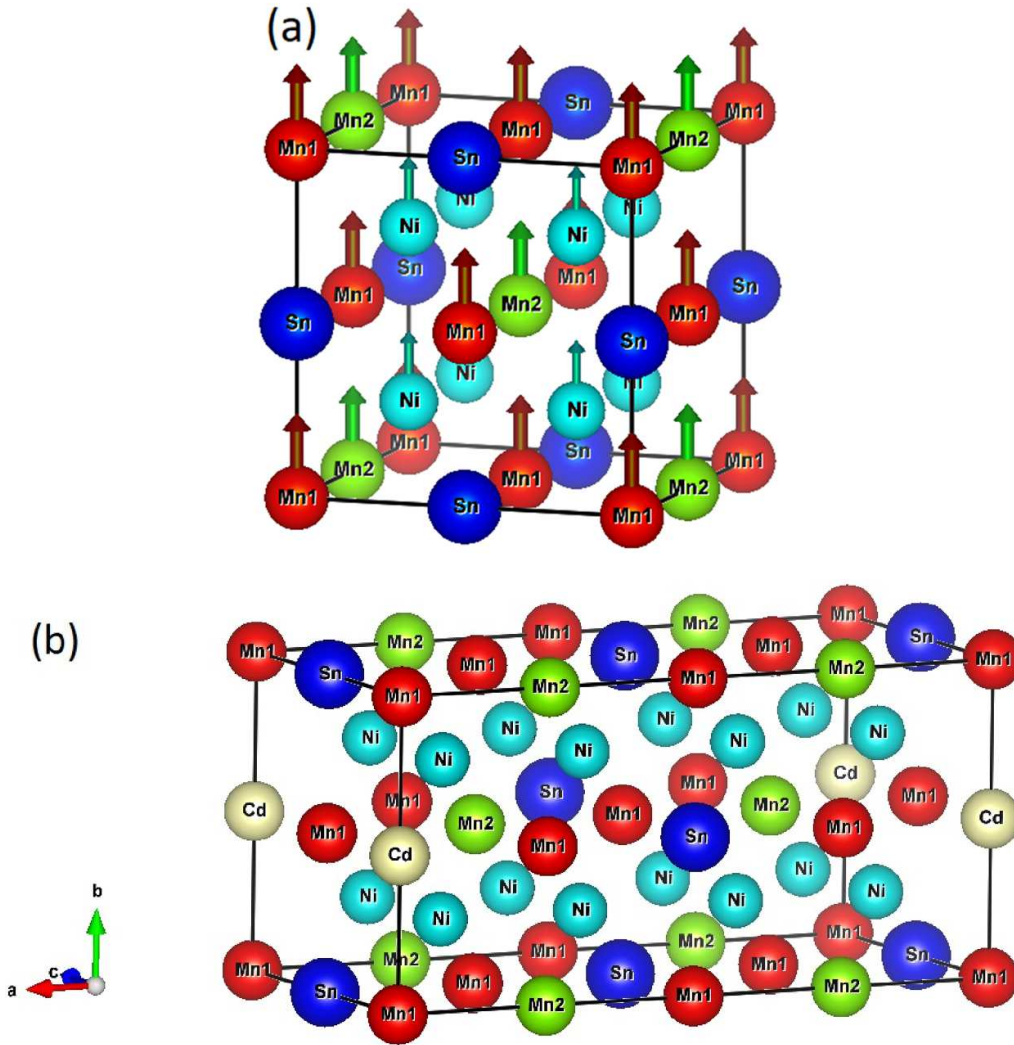


Figure 7. (a) 16-atom supercell for Ni₈Mn₆Sn₂ Heusler-type alloy with FM configuration of the magnetic moments; (b) 32-atom supercell of Ni₁₆Mn₁₂Sn₃Cd₁ alloy with the same magnetic configuration; magnetic moments are not shown in this case to avoid overlapping.

Table 3. Computed lattice parameters, total per formula unit, and atomic magnetic moments (in Bohr magneton) for Ni₈Mn₆Sn₂ and Ni₁₆Mn₁₂Sn₃Cd₁ in the cubic and tetragonal phases in the FM and AFM configurations.

Alloy	Lattice parameter (Å)	$\mu_{\text{Cal}}^{\text{Tot}} (\mu_B/f.u.)$	$\mu_{\text{Exp}}^{\text{Tot}} (\mu_B/f.u.)$	$\mu^{\text{Ni}} (\mu_B)$	$\mu^{\text{Mn1}} (\mu_B)$	$\mu^{\text{Mn2}} (\mu_B)$	$\mu^{\text{Sn}} (\mu_B)$	$\mu^{\text{Cd}} (\mu_B)$
Ni ₈ Mn ₆ Sn ₂ (FM)	6.034	7.00		0.47	3.88	3.92	-0.03	—
Ni ₈ Mn ₆ Sn ₂ (FM)(c/a = 1.200)	5.673 5.673 6.808	6.92		0.50	3.87	3.95	-0.04	—
Ni ₈ Mn ₆ Sn ₂ (AFM)	6.029	2.13		0.12	3.92	-4.05	-0.03	—
Ni ₈ Mn ₆ Sn ₂ (AFM)(c/a = 1.210)	5.662 5.662 6.795	2.26	1.98	0.21	3.87	-4.01	-0.04	—
Ni ₁₆ Mn ₁₂ Sn ₃ Cd ₁ (FM)	6.020	6.98		0.50	3.90	3.92	-0.03	-0.02
Ni ₁₆ Mn ₁₂ Sn ₃ Cd ₁ (FM)(c/a = 1.200)	5.665 5.665 6.798	6.91		0.50	3.87	3.92	-0.04	-0.03
Ni ₁₆ Mn ₁₂ Sn ₃ Cd ₁ (AFM)	6.016	2.20		0.14	3.91	-4.01	-0.03	-0.01
Ni ₁₆ Mn ₁₂ Sn ₃ Cd ₁ (AFM)(c/a = 1.210)	5.662 5.662 6.794	2.28	1.66	0.20	3.89	-4.01	-0.04	-0.01

not agree with the experimental results [27, 31, 79, 80]. This incompatibility is attributed to factors such as the atomic disorder and/or zero Kelvin calculations. The obtained results solve the mentioned discrepancy by adding the U Hubbard correction tool to the computations. Therefore, it is shown that the FM configuration of the cubic phase is more stable than AFM for both undoped and Cd-doped alloys, in agreement with the experimental results. The computed equilibrium lattice constants for the FM cubic phase are 6.034 Å and 6.020 Å for the undoped and Cd-doped alloys, respectively. Although introducing the U Hubbard correction to the model recognizes the stable magnetic state, it leads to overestimating the lattice parameter [81]. Nevertheless, based on table 3, the computed lattice parameters are very close to the experimental ones (5.993 Å and 5.983 Å for undoped and doped alloys, respectively). Furthermore, table 3 illustrates a reduction of the lattice parameters by Cd doping obtained both experimentally and theoretically.

The magnetic moment of Ni depends on Z elements [82]. As deduced from table 3, its slight increase can be attributed to the stronger FM coupling with the neighboring atoms. The magnetic moments of Mn1 and Mn2 did not change noticeably, which can be related to the minor influence of Cd-doping. While the neighboring atoms get closer to each other, the FM interaction passes through the maximum of the FM coupling. It then decreases being replaced by the AFM coupling due to the reduced Mn–Mn interatomic distances. Regarding the two magnetic configurations FM and AFM, and changeable Mn–Mn distances, its magnetic moments of Mn can decrease or increase. Since Cd substitution shows a minor influence on Mn and Ni moments, the total change of the magnetic moment is small (7.00 $\mu_B/f.u.$ without and 6.98 $\mu_B/f.u.$ with 1 at.% Cd dopant). The sizeable total moment mainly comes from the contribution of the Mn atoms. A small negative value of the moment on Sn- and Cd-sites is observed. The small contributions of the Cd moments can be related to its low lying *d* states, which do not hybridize directly with the *d* states of other atoms [83].

We obtained the optimal geometrical structure by calculating the total energy per unit cell at different lattice constants for the FM and AFM states in the cubic austenite phase to gain insight into the ground state of the alloys. The equilibrium lattice constants were derived corresponding to the minimum energy. As seen in figure 8, the total energy of the FM state has lower energy than that of the AFM around the equilibrium state for both undoped and Cd-doped alloys. The energy difference between FM and AFM configurations is as high as 7.127 meV/atom in the undoped alloy and decreases in value to 1.170 meV/atom for the Cd1Sn alloy. Consequently, FM interactions in the undoped alloy are stronger than in the Cd-doped one. The calculation of exchange parameters is needed for a more detailed investigation, which is not considered in the present article. As mentioned in the experimental section, the total magnetic configuration in MetaMSMAs is the result of competition between AFM interaction of Mn1–Mn2 and FM interaction of Mn1–Mn1 and Ni–Mn1, that is strongly dependent on the lattice parameters and the conduction electrons of

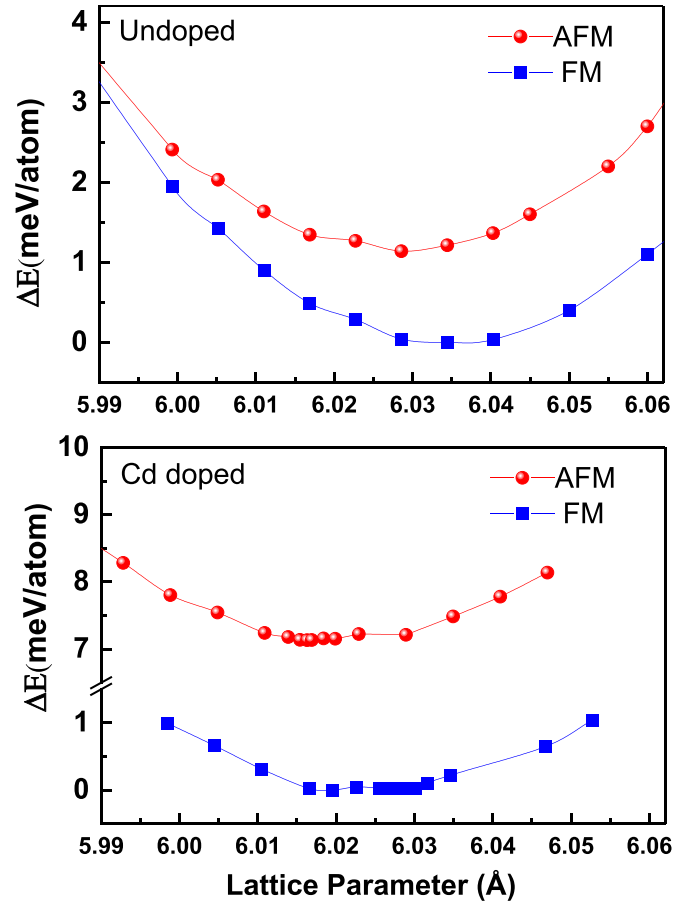


Figure 8. Variation of the total energy as a function of the lattice parameter for undoped and Cd-doped alloys with FM and AFM configurations.

a Z constituent in Ni–Mn–Z (Z=In, Sn, ...) Heusler alloys [84, 85].

The total energy as a function of the tetragonality ratio, c/a , is calculated while utilizing the relaxation of atomic positions by keeping constant the unit cell volume of the cubic structure ($V=a^3$). Finally, at the minima of energies for particular values of c/a , the full relaxation, which included the atomic positions and unit cell lattice parameters, was carried out.

It is worth mentioning that the small volume change between austenite and martensite is considered in some materials. Wu *et al* [86] investigated the influence of volume on the tetragonal distortion by applying constant strain to Pd₂FeSe, Pd₂MnSe, Pd₂MnTe, and Pd₂FeTe alloys. Their investigation revealed that the uniform expansion from optimized volume causes the absolute value of the total energy of the tetragonal phase to decrease. In contrast, the contraction of the optimized volume of the tetragonal lattice leads to a higher absolute value of the total energy. In other words, the absolute value of ΔE and $V_{opt} + X\%V_{opt}$ are inversely correlated. Moreover, it was shown that whether the volume changes or not, the c/a ratio of the individual alloy remains constant [86]. Different behavior was reported by Luo *et al* [87]. They showed that in the Ni₂MnGe alloy, a slight contraction or expansion of the

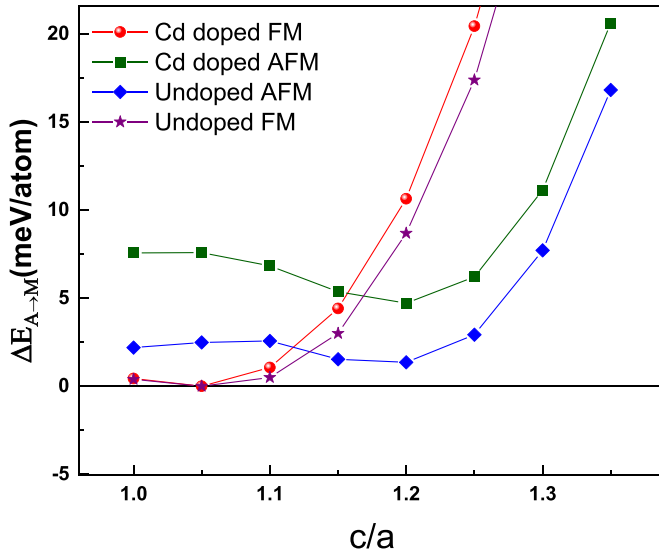


Figure 9. Variation of the total energy as a function of tetragonal ratio, c/a , for undoped and Cd-doped alloys with FM and AFM configurations.

unit cell has led to the energy increase compared to the situation with the fixed cell volume change [87]. Furthermore, no cell volume change was considered between the two phases in many FM shape memory alloys, such as Mn_2NiGa and Ni_2MnGa . In the present article, it was assumed that the same constant cell volume for the austenitic and martensitic phases; investigating the effect of volume change is beyond the scope of this article [87].

Figure 9 shows the energy difference profile as a function of tetragonal distortions for the FM and AFM configurations. The energy of the FM $L2_1$ phase is considered as the reference. Since the reference is the total energy of the cubic austenitic phase ($c/a = 1$), it is evident that the total energy of the martensitic phase is smaller than the austenitic one. The difference in energy between the austenitic and martensitic phases ($\Delta E = E_{\text{Cub}} - E_{\text{Tetra}}$) is calculated since it is an important qualitative parameter to predict MT. In general, the higher ΔE implies higher temperature of MT. Therefore, estimation of the MT temperature can be done using the depth of the tetragonality valley due to the correlation of energy and MT temperature ($E = K_B T$) [88]. The values of ΔE corresponding to Cd_0Sn and Cd_1Sn indicate that these alloys exhibit tetragonal distortions, as evident by the existence of MT in the experimental section. More importantly, the higher the value of ΔE , the more probable the structural transformation will happen, and the more stable the corresponding tetragonal structure is.

Cd-doping enhances the total energy difference. Therefore, the increase of MT temperature is observed by Cd substitution due to the deeper minima in this case. This enhancement is in agreement with our experimental results. Cd-dopant deepens the minimum of the AFM state and simultaneously lowers the FM state energy compared to the undoped sample. According to figure 9, the FM configuration is more stable in the cubic structure ($c/a = 1$), as expected in the austenite phase; with increasing c/a ratio, the minimum energy corresponds to AFM

configuration around $c/a = 1.210$, which means the existence of MT. So, the stability of the AFM configuration rather than the FM is a sign of the MT occurrence. Modified Mn–Mn distances, as a result of MT, cause additional AFM correlations that stabilize the weak magnetic state of martensite [88]. The austenite phase must be in the FM state, and martensite must be in the AFM configuration to assure adequate driving force for the reverse MT [82].

From the electronic point of view, it is interesting to consider the role of the Sn element, representative of the main group in the periodic table, and d -metals, particularly Zn and Cd. As Ni *et al* [89] reported, in all d -metal Heusler alloys, Zn shows an isolated DOS peak in the d state that is quite sharp and less populated. It originates from the contributions of Zn $3d$ states. The s states of Zn are located far below the Fermi level. In contrast, the p states are encountered in the region much closer to the Fermi energy. As a result, a hybridization among the p states of Zn and d states of other transition metals can happen, similar to the p - d hybridization in classic Heusler alloys between transition metals and atoms of the main group. Therefore, the Zn atom may be considered as playing the same role as the main group element. Due to the similar electronic configurations of Cd ($4d^{10} 5s^2$) and Zn ($3d^{10} 4s^2$) in the computations, we can conclude that the role of Cd should be similar to the role of Sn; the latter one is representative of the main group elements. This leads to the reasonable assumption that p -orbitals of d -metals, such as Cd (the present work) or Zn ([37].), might play the same role as p -orbitals of Sn. DOS of Zn shows that s - and p -orbitals near the Fermi level strongly influence p - d hybridization [83, 90]. Since the fully occupied d state and its low energy, the indirect interaction between Cd electronic states and those of another transition metal in the Heusler alloys should exist. Therefore, the Cd atom may be considered as playing the same role as the main group element, Sn, in Ni–Mn–Sn MetaMSMAs.

4. Summary

The effect of Cd-doping in Ni–Mn–Sn MetaMSMAs was explored experimentally and theoretically. By studying the transformation behavior, magnetic properties, and inverse MCE, it was shown that the Cd acts as an effective element to optimize the MT and MCE parameters in the $\text{Ni}_{47}\text{Mn}_{40}\text{Sn}_{13-x}\text{Cd}_x$ ($x = 0, 0.75, 1, 1.25$ at. %) MetaMSMAs.

The experimental and theoretical results illustrated that increasing Cd doping reduces the unit cell volume, potentially a thermodynamic reason for the substantial increase of the MT temperature. Nevertheless, further analysis showed that the e/a ratio plays a more significant role in enhancing the MT temperature than the unit cell volume.

The DFT computations showed that the ground state of the alloys is a tetragonal structure with $c/a = 1.210$, confirming that these alloys experience MT. Furthermore, the difference in the total energy of the cubic and tetragonal phases controls the MT temperature that increases with the amount of Cd dopant, in agreement with the experiment.

Two different spin configurations, FM, and AFM, were computed by DFT + U Hubbard model. It was proved that the FM state is energetically more favorable than AFM for both undoped and Cd-doped alloys in the cubic phase, solving the discrepancies reported in the previous literature.

MCE was investigated by the direct measurements of ΔT_{ad} under a magnetic field of 1.96 T and indirect measurements under different magnetic fields up to 5 T. The results of direct and indirect measurements of MCE in the vicinity of MT showed that the addition of Cd as a nonmagnetic 4d transition metal to the ternary Ni–Mn–Sn alloy not only improves ΔT_{ad} and ΔS_M but also increases the MT temperature to near room temperature. Furthermore, the direct measurement shows that Cd-doping enhances ΔT_{ad} at 1.96 T from 0.9 K for the undoped alloy to 1.6 K for the doped one, which is nearly 78% improvement. The latter value agrees with the literature data on MetaMSMAs, offering Cd-doped alloys as promising candidates for magnetic refrigeration.

Data availability statement

The data that support the findings of this study are available upon reasonable request from the authors.

Acknowledgments

This work was supported by the Isfahan University of Technology (IUT). The authors would like to thank Iran National Science Foundation (INSF) for this project's financial support (Project No. 4000228). The financial support of the Spanish Ministry of Science, Innovation and Universities (Project RTI2018-094683-B-C53-54) and Basque Government Department of Education (Project IT1245-19) is acknowledged. DV acknowledges partial support by NSF under Grant Nos. ECCS-1711253 and CBET-2110603. Computational resources are provided by Westgrid.

Conflict of interest

The authors declare that they have no known competing financial interests or personal relationships that could have appeared to influence the work reported in this paper.

ORCID iDs

Z Ghazinezhad  <https://orcid.org/0000-0002-1100-4264>
 P Kameli  <https://orcid.org/0000-0003-4490-0767>
 A Ghotbi Varzaneh  <https://orcid.org/0000-0002-1448-5008>
 I Abdolhosseini Sarsari  <https://orcid.org/0000-0001-5825-0086>
 M Norouzi-Inallu  <https://orcid.org/0000-0003-0044-9177>
 T Amiri  <https://orcid.org/0000-0001-6986-8164>
 D Salazar  <https://orcid.org/0000-0002-2149-3268>

D Vashaee  <https://orcid.org/0000-0003-3667-3672>
 V Chernenko  <https://orcid.org/0000-0002-0933-9372>

References

- [1] L'vov V A, Kosogor A, Barandiaran J M and Chernenko V A 2016 Theoretical description of magnetocaloric effect in the shape memory alloy exhibiting metamagnetic behavior *J. Appl. Phys.* **119** 013902
- [2] Liu J *et al* 2019 Reversible low-field magnetocaloric effect in Ni–Mn–In-based Heusler alloys *Phys. Rev. Mater.* **3** 084409
- [3] Kosogor A, Barandiaran J M, L'vov V A, Fernandez J R and Chernenko V A 2017 Magnetic and nonmagnetic contributions to the heat capacity of metamagnetic shape memory alloy *J. Appl. Phys.* **121** 183901
- [4] Pecharsky V K and Gschneidner Jr K A 1997 Giant magnetocaloric effect in Gd₅(Si₂Ge₂) *Phys. Rev. Lett.* **78** 4494
- [5] Yibole H, Guillou F, Zhang L, Van Dijk N and Brück E 2014 Direct measurement of the magnetocaloric effect in MnFe (P, X)(X = As, Ge, Si) materials *J. Phys. D: Appl. Phys.* **47** 075002
- [6] Shao Y *et al* 2017 High-performance solid-state cooling materials: balancing magnetocaloric and non-magnetic properties in dual phase La–Fe–Si *Acta Mater.* **125** 506–12
- [7] Liu J, Skokov K and Gutfleisch O 2012 Magnetostructural transition and adiabatic temperature change in Mn–Co–Ge magnetic refrigerants *Scr. Mater.* **66** 642–5
- [8] Chirkova A, Skokov K, Schultz L, Baranov N, Gutfleisch O and Woodcock T 2016 Giant adiabatic temperature change in FeRh alloys evidenced by direct measurements under cyclic conditions *Acta Mater.* **106** 15–21
- [9] Buchelnikov V and Sokolovskiy V 2011 Magnetocaloric effect in Ni–Mn–X (X = Ga, In, Sn, Sb) Heusler alloys *Phys. Met. Metallography* **112** 633–65
- [10] Ma Z, Dong X, Zhang Z and Li L 2021 Achievement of promising cryogenic magnetocaloric performances in La_{1-x}Pr_xFe₁₂B₆ compounds *J. Mater. Sci. Technol.* **92** 138–42
- [11] Zhang Y, Zhu J, Li S, Wang J and Ren Z 2022 Achievement of giant cryogenic refrigerant capacity in quinary rare-earths based high-entropy amorphous alloy *J. Mater. Sci. Technol.* **102** 66–71
- [12] Li L *et al* 2020 Magnetic properties and excellent cryogenic magnetocaloric performances in B-site ordered RE₂ZnMnO₆ (RE = Gd, Dy and Ho) perovskites *Acta Mater.* **194** 354–65
- [13] Wu B, Zhang Y, Guo D, Wang J and Ren Z 2021 Structure, magnetic properties and cryogenic magneto-caloric effect (MCE) in RE₂FeAlO₆ (RE = Gd, Dy, Ho) oxides *Ceram. Int.* **47** 6290–7
- [14] Zhang Y *et al* 2022 Magnetic properties and giant cryogenic magnetocaloric effect in B-site ordered antiferromagnetic Gd₂MgTiO₆ double perovskite oxide *Acta Mater.* **226** 117669
- [15] Guo D *et al* 2021 First- and second-order phase transitions in RE₆Co₂Ga (RE = Ho, Dy or Gd) cryogenic magnetocaloric materials *Sci. China Mater.* **64** 2846–57
- [16] Li L and Yan M 2020 Recent progresses in exploring the rare earth based intermetallic compounds for cryogenic magnetic refrigeration *J. Alloys Compd.* **823** 153810
- [17] Zhang Y 2019 Review of the structural, magnetic and magnetocaloric properties in ternary rare earth RE₂T₂X type intermetallic compounds *J. Alloys Compd.* **787** 1173–86
- [18] Caron L, Devi P, Carvalho A M, Felser C and Singh S 2018 Minimizing hysteresis in martensite phase transforming magnetocaloric Heusler alloys (arXiv:1806.05075)

- [19] Feng-Xia H, Bao-Gen S and Ji-Rong S 2013 Magnetic entropy change involving martensitic transition in NiMn-based Heusler alloys *Chin. Phys. B* **22** 037505
- [20] Krenke T et al 2005 Inverse magnetocaloric effect in ferromagnetic Ni–Mn–Sn alloys *Nat. Mater.* **4** 450–4
- [21] Norouzi-Inallu M et al 2022 Influence of W Doping on the structure, magnetism and exchange bias in $\text{Ni}_{47}\text{Mn}_{40}\text{Sn}_{13-x}\text{W}_x$ Heusler alloys *J. Phys.: Condens. Matter*
- [22] Khan M, Pathak A K, Paudel M R, Dubenko I, Stadler S and Ali N 2008 Magneto-resistance and field-induced structural transitions in $\text{Ni}_{50}\text{Mn}_{50-x}\text{Sn}_x$ Heusler alloys *J. Magn. Mater.* **320** L21–L25
- [23] Ullakko K, Huang J, Kantner C, O’handley R and Kokorin V 1996 Large magnetic-field-induced strains in Ni_2MnGa single crystals *Appl. Phys. Lett.* **69** 1966–8
- [24] Esakki Muthu S et al 2013 Influence of Si substitution on the structure, magnetism, exchange bias and negative magnetoresistance in $\text{Ni}_{48}\text{Mn}_{39}\text{Sn}_{13}$ Heusler alloys *J. Phys. D: Appl. Phys.* **46** 205001
- [25] Varzaneh A G et al 2017 Effect of Cu substitution on magnetocaloric and critical behavior in $\text{Ni}_{47}\text{Mn}_{40}\text{Sn}_{13-x}\text{Cu}_x$ alloys *J. Alloys Compd.* **708** 34–42
- [26] Entel P et al 2012 First-principles investigations of caloric effects in ferroic materials *AIP Conf. Proc.* **1461** 11–23
- [27] Li C-M, Hu Q-M, Yang R, Johansson B and Vitos L 2013 Magnetic ordering and physical stability of $\text{X}_2\text{Mn}_{1+x}\text{Sn}_{1-x}$ (X= Ru, Os, Co, Rh, Ni, Pd, Cu, and Ag) Heusler alloys from a first-principles study *Phys. Rev. B* **88** 014109
- [28] Li C-M, Luo H-B, Hu Q-M, Yang R, Johansson B and Vitos L 2012 Role of magnetic and atomic ordering in the martensitic transformation of Ni-Mn-In from a first-principles study *Phys. Rev. B* **86** 214205
- [29] Sokolovskiy V, Buchelnikov V, Zagrebina M, Entel P, Sahoo S and Ogura M 2012 First-principles investigation of chemical and structural disorder in magnetic $\text{Ni}_2\text{Mn}_{1+x}\text{Sn}_{1-x}$ Heusler alloys *Phys. Rev. B* **86** 134418
- [30] Buchelnikov V et al 2010 First-principles and Monte Carlo study of magnetostructural transition and magnetocaloric properties of $\text{Ni}_{2+x}\text{Mn}_{1-x}\text{Ga}$ *Phys. Rev. B* **81** 094411
- [31] Sokolovskiy V, Zagrebina M and Buchelnikov V D 2018 Magnetocaloric effect in Ni-Co-Mn-(Sn, Al) Heusler alloys: theoretical study *J. Magn. Mater.* **459** 295–300
- [32] Zagrebina M A, Sokolovskiy V V and Buchelnikov V D 2017 *Ab initio* calculations of structural and magnetic properties of Ni-Co-Mn-Cr-Sn supercell *Intermetallics* **87** 55–60
- [33] Wang X, Shang J-X, Wang F-H, Jiang C-B and Xu H-B 2014 Origin of unusual properties in the ferromagnetic Heusler alloy Ni–Mn–Sn: a first-principles investigation *Scr. Mater.* **89** 33–36
- [34] Li C, van de Bovenkamp R and Van Mieghem P 2012 Susceptible-infected-susceptible model: a comparison of N-intertwined and heterogeneous mean-field approximations *Phys. Rev. E* **86** 026116
- [35] Li C-M, Hu Q-M, Yang R, Johansson B and Vitos L 2015 Theoretical investigation of the magnetic and structural transitions of Ni-Co-Mn-Sn metamagnetic shape-memory alloys *Phys. Rev. B* **92** 024105
- [36] Xiao H, Yang C, Wang R, Xu L, Liu G and Marchenkov V 2016 First-principles study of martensitic transformation and magnetic properties of carbon doped Ni–Mn–Sn Heusler alloys *Phys. Lett. A* **380** 3414–20
- [37] Varzaneh A G et al 2020 Magnetic and magnetocaloric properties of $\text{Ni}_{47}\text{Mn}_{40}\text{Sn}_{13-x}\text{Zn}_x$ alloys: direct measurements and first-principles calculations *Phys. Rev. B* **101** 134403
- [38] Bhatti K P, El-Khatib S, Srivastava V, James R and Leighton C 2012 Small-angle neutron scattering study of magnetic ordering and inhomogeneity across the martensitic phase transformation in $\text{Ni}_{50-x}\text{Co}_x\text{Mn}_{40}\text{Sn}_{10}$ alloys *Phys. Rev. B* **85** 134450
- [39] Han Z et al 2012 Martensitic transformation and magnetocaloric effect in Mn–Ni–Nb–Sn shape memory alloys: the effect of 4d transition-metal doping *J. Alloys Compd.* **515** 114–8
- [40] Ram N R et al 2018 Review on magnetocaloric effect and materials *J. Supercond. Novel Magn.* **31** 1971–9
- [41] Franco V, Blázquez J, Ipus J, Law J, Moreno-Ramírez L and Conde A 2018 Magnetocaloric effect: from materials research to refrigeration devices *Prog. Mater. Sci.* **93** 112–232
- [42] Varzaneh A G, Kameli P, Zahedi V, Karimzadeh F and Salamati H 2015 Effect of heat treatment on martensitic transformation of $\text{Ni}_{47}\text{Mn}_{40}\text{Sn}_{13}$ ferromagnetic shape memory alloy prepared by mechanical alloying *Met. Mater. Int.* **21** 758–64
- [43] Álvarez-Alonso P et al 2015 Simple set-up for adiabatic measurements of magnetocaloric effect *Key Engineering Materials* vol 644 (Bâch: Trans Tech Publications) pp 215–8
- [44] Garrity K F, Bennett J W, Rabe K M and Vanderbilt D 2014 Pseudopotentials for high-throughput DFT calculations *Comput. Mater. Sci.* **81** 446–52
- [45] Perdew J P, Burke K and Ernzerhof M 1996 Generalized gradient approximation made simple *Phys. Rev. Lett.* **77** 3865
- [46] Momma K and Izumi F 2011 VESTA 3 for three-dimensional visualization of crystal, volumetric and morphology data *J. Appl. Crystallogr.* **44** 1272–6
- [47] Taubel A et al 2018 A comparative study on the magnetocaloric properties of Ni-Mn-X (-Co) Heusler Alloys *Phys. Status Solidi B* **255** 1700331
- [48] Huang L et al 2015 Large magnetic entropy change and magnetoresistance in a $\text{Ni}_{41}\text{Co}_9\text{Mn}_{40}\text{Sn}_{10}$ magnetic shape memory alloy *J. Alloys Compd.* **647** 1081–5
- [49] White B D, Barabash R, Barabash O, Jeon I and Maple M 2019 Magnetocaloric effect near room temperature in quinary and sextenary Heusler alloys *J. Appl. Phys.* **126** 165101
- [50] Gamzatov A, Aliev A, Ghotbi Varzaneh A, Kameli P, Abdolhosseini Sarsari I and Yu S 2018 Inverse-direct magnetocaloric effect crossover in $\text{Ni}_{47}\text{Mn}_{40}\text{Sn}_{12.5}\text{Cu}_{0.5}$ Heusler alloy in cyclic magnetic fields *Appl. Phys. Lett.* **113** 172406
- [51] Sharma J, Coelho A, Repaka D, Ramanujan R and Suresh K 2019 Pressure induced martensitic transition, magnetocaloric and magneto-transport properties in Mn-Ni-Sn Heusler alloy *J. Magn. Mater.* **487** 165307
- [52] Lázpita P, Sasmaz M, Cesari E, Barandiarán J, Gutiérrez J and Chernenko V 2016 Martensitic transformation and magnetic field induced effects in $\text{Ni}_{42}\text{Co}_8\text{Mn}_{39}\text{Sn}_{11}$ metamagnetic shape memory alloy *Acta Mater.* **109** 170–6
- [53] Chernenko V A, L’vov V A, Cesari E and Barandiarán J M 2019 Fundamentals of magnetocaloric effect in magnetic shape memory alloys *Handbook of Magnetic Materials* vol **28** (Amsterdam: Elsevier) pp 1–45
- [54] Devi P, Mejía C S, Caron L, Singh S, Nicklas M and Felser C 2019 Effect of chemical and hydrostatic pressure on the coupled magnetostructural transition of Ni-Mn-In Heusler alloys *Phys. Rev. Mater.* **3** 122401
- [55] Diestel A, Niemann R, Schleicher B, Nielsch K and Fähler S 2018 Reducing hysteresis losses by heating minor loops in magnetocaloric Ni–Mn–Ga–Co Films *Energy Technol.* **6** 1463–9
- [56] Gottschall T, Stern-Taulats E, Mañosa L, Planes A, Skokov K P and Gutfleisch O 2017 Reversibility of minor hysteresis loops in magnetocaloric Heusler alloys *Appl. Phys. Lett.* **110** 223904

- [57] Wei Z *et al* 2015 Realization of multifunctional shape-memory ferromagnets in all-d-metal Heusler phases *Appl. Phys. Lett.* **107** 022406
- [58] Ghosh A, Sen P and Mandal K 2016 Measurement protocol dependent magnetocaloric properties in a Si-doped Mn-rich Mn-Ni-Sn-Si off-stoichiometric Heusler alloy *J. Appl. Phys.* **119** 183902
- [59] Orlandi F, Çakır A, Manuel P, Khalyavin D D, Acet M and Righi L 2020 Neutron diffraction and symmetry analysis of the martensitic transformation in Co-doped Ni₂ MnGa *Phys. Rev. B* **101** 094105
- [60] Kirat G and Aksan M 2021 Influence of the Cu substitution on magnetic properties of Ni–Mn–Sn–B shape memory ribbons *Appl. Phys. A* **127** 1–9
- [61] Krenke T, Acet M, Wassermann E F, Moya X, Mañosa L and Planes A 2006 Ferromagnetism in the austenitic and martensitic states of Ni–Mn–In alloys *Phys. Rev. B* **73** 174413
- [62] Pathak A K, Khan M, Gautam B R, Stadler S, Dubenko I and Ali N 2009 Exchange bias in bulk Ni–Mn–In-based Heusler alloys *J. Magn. Magn. Mater.* **321** 963–5
- [63] Khan M, Dubenko I, Stadler S and Ali N 2007 Exchange bias behavior in Ni–Mn–Sb heusler alloys *Appl. Phys. Lett.* **91** 072510
- [64] Wang H *et al* 2020 Effect of Ti doping on the phase transitions, magnetocaloric effect, and exchange bias in Ni₄₃Mn₄₆Sn_{11–x}Ti_x Heusler alloys *J. Magn. Magn. Mater.* **498** 166216
- [65] Raji G *et al* 2016 Martensitic transition, spin glass behavior and enhanced exchange bias in Si substituted Ni₅₀ Mn₃₆ Sn₁₄ Heusler alloys *RSC Adv.* **6** 32037–45
- [66] Machavarapu R and Jakob G 2013 Exchange bias effect in the martensitic state of Ni-Co-Mn-Sn film *Appl. Phys. Lett.* **102** 232406
- [67] Pecharsky V and Gschneidner K Jr 1999 Magnetocaloric effect from indirect measurements: magnetization and heat capacity *J. Appl. Phys.* **86** 565–75
- [68] Inallu M N *et al* 2019 Magnetocaloric effect in W-doped Ni–Mn–Sn alloy probed by direct and indirect measurements *J. Appl. Phys.* **52** 235001
- [69] Gottschall T 2016 On the magnetocaloric properties of Heusler compounds: reversible, time- and size-dependent effects of the martensitic phase transition
- [70] Ghorbani Zavareh M *et al* 2015 Direct measurements of the magnetocaloric effect in pulsed magnetic fields: the example of the Heusler alloy Ni₅₀Mn₃₅In₁₅ *Appl. Phys. Lett.* **106** 071904
- [71] Gottschall T, Skokov K P, Benke D, Gruner M E and Gutfleisch O 2016 Contradictory role of the magnetic contribution in inverse magnetocaloric Heusler materials *Phys. Rev. B* **93** 184431
- [72] Kihara T, Xu X, Ito W, Kainuma R and Tokunaga M 2014 Direct measurements of inverse magnetocaloric effects in metamagnetic shape-memory alloy NiCoMnIn *Phys. Rev. B* **90** 214409
- [73] Wójcik A *et al* 2017 Transformation behavior and inverse caloric effects in magnetic shape memory Ni_{44–x}Cu_xCo₆Mn₃₉Sn₁₁ ribbons *J. Alloys Compd.* **721** 172–81
- [74] Álvarez-Alonso P, Aguilar-Ortiz C O, Camarillo J, Salazar D, Flores-Zúñiga H and Chernenko V 2016 Adiabatic magnetocaloric effect in Ni₅₀Mn₃₅In₁₅ ribbons *Appl. Phys. Lett.* **109** 212402
- [75] Çakır Ö and Acet M 2012 Reversibility in the inverse magnetocaloric effect in Mn₃GaC studied by direct adiabatic temperature-change measurements *Appl. Phys. Lett.* **100** 202404
- [76] Han Y, Wu M, Kuang M, Yang T, Chen X and Wang X 2018 All-d-metal equiatomic quaternary Heusler hypothetical alloys ZnCdTMn (T= Fe, Ru, Os, Rh, Ir, Ni, Pd, Pt): a first-principle investigation of electronic structures, magnetism, and possible martensitic transformations *Results Phys.* **11** 1134–41
- [77] Wei X-P *et al* 2011 A first principles study on the full-Heusler compound Mn₂CuSb *Comput. Mater. Sci.* **50** 1175–8
- [78] Priolkar K *et al* 2013 Antiferromagnetic exchange interactions in the Ni₂ Mn_{1.4} In_{0.6} ferromagnetic Heusler alloy *Phys. Rev. B* **87** 144412
- [79] Grünebohm A, Herper H C and Entel P 2016 On the rich magnetic phase diagram of (Ni, Co)–Mn–Sn Heusler alloys *J. Phys. D: Appl. Phys.* **49** 395001
- [80] Singh V, van Rookeghem A, Panda S, Majumdar S, Mingo N and Dasgupta I 2018 Magnetic order and lattice instabilities in Ni₂Mn_{1+x}Sn_{1–x} Heusler based magnetic shape-memory alloys (arXiv:1811.04221)
- [81] Zelený M, Straka L, Rameš M, Sozinov A and Heczko O 2020 Origin of magnetocrystalline anisotropy in Ni–Mn–Ga–Co–Cu tetragonal martensite *J. Magn. Magn. Mater.* **503** 166522
- [82] He W, Huang H, Liu Z and Ma X 2017 First-principles investigation of magnetic properties and metamagnetic transition of NiCoMnZ (Z= In, Sn, Sb) Heusler alloys *Intermetallics* **90** 140–6
- [83] Ni Z, Ma Y, Liu X, Luo H, Liu H and Meng F 2018 Electronic structure, magnetic properties and martensitic transformation in all-d-metal Heusler alloys Zn₂YMn (Y= Fe, Co, Ni, Cu) *J. Magn. Magn. Mater.* **451** 721–6
- [84] Şaşıoğlu E, Sandratskii L and Bruno P 2006 Magnetic phase diagram of the semi-Heusler alloys from first principles *Appl. Phys. Lett.* **89** 222508
- [85] Şaşıoğlu E, Sandratskii L and Bruno P 2008 Role of conduction electrons in mediating exchange interactions in Mn-based Heusler alloys *Phys. Rev. B* **77** 064417
- [86] Wu M *et al* 2019 Competition of L21 and L10 ordering in Pd₂MnSe, Pd₂FeSe, Pd₂MnTe and Pd₂FeTe Heusler alloys *Results Phys.* **12** 1398–404
- [87] Luo H *et al* 2013 Electronic structure and possible martensitic transformation in Mn₂NiGe and Ni₂MnGe *Intermetallics* **38** 139–43
- [88] Gruenebohm A, Comtesse D, Hucht A, Gruner M E, Maslovskaya A and Entel P 2014 Optimizing the magnetocaloric effect in Ni–Mn–Sn by substitution: a first-principles study *IEEE Trans. Magn.* **50** 2506004
- [89] Ni Z, Guo X, Li Q, Liang Z, Luo H and Meng F 2018 Effect of Zn-doping on the phase transition and magnetic properties of Heusler alloys Ni₂MnGa_{1–x}Zn_x (x= 0, 0.25, 0.5, 0.75 and 1) *J. Magn. Magn. Mater.* **464** 65–70
- [90] Wang X, Wu M, Yang T and Khenata R 2020 Effect of Zn doping on phase transition and electronic structures of Heusler-type Pd₂ Cr-based alloys: from normal to all-d-metal Heusler *RSC Adv.* **10** 17829–35